Joule

CellPress

Article

Layer-by-Layer Degradation of Methylammonium Lead Tri-iodide Perovskite Microplates

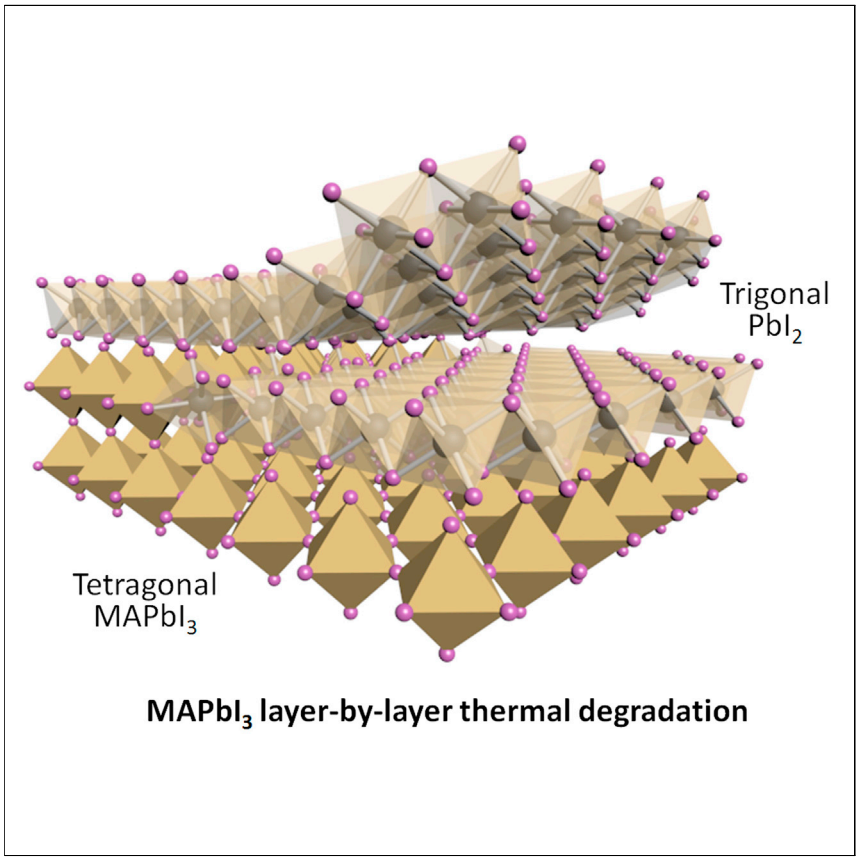

In situ TEM study reveals the atomistic structural evolution in perovskite material under moderate heating, for the first time revealing a surface-initiated layer-by-layer degradation model. Along with theoretical calculations, the study offers important insight regarding structural evolution and suggests effective strategies to improve the stability of perovskite materials.

Zheng Fan, Hai Xiao, Yiliu Wang, ..., William A. Goddard III, Yu Huang, Xiangfeng Duan

wag@wag.caltech.edu (W.A.G.)
yhuang@seas.ucla.edu (Y.H.)
xduan@chem.ucla.edu (X.D.)

HIGHLIGHTS

An *in situ* TEM study reveals atomistic pathway of thermal degradation in $MAPbI_3$

A surface reaction initiated layer-by-layer degradation model is discovered

Encapsulation by BN can restrain the surface reaction and retard the degradation

Theoretical calculations confirm the encapsulation slows down degradation rate

Fan et al., Joule 1, 548–562
November 15, 2017 © 2017 Elsevier Inc.
http://dx.doi.org/10.1016/j.joule.2017.08.005

CrossMark

Joule

CellPress

Article

Layer-by-Layer Degradation of Methylammonium Lead Tri-iodide Perovskite Microplates

Zheng Fan,[1,2,5] Hai Xiao,[3,5] Yiliu Wang,[2] Zipeng Zhao,[1] Zhaoyang Lin,[2] Hung-Chieh Cheng,[1] Sung-Joon Lee,[1] Gongming Wang,[2] Ziying Feng,[2] William A. Goddard III,[3,*] Yu Huang,[1,4,*] and Xiangfeng Duan[2,4,6,*]

SUMMARY

The methylammonium lead iodide ($MAPbI_3$) perovskite has attracted considerable interest for its high-efficiency, low-cost solar cells, but is currently plagued by its poor environmental and thermal stability. To aid the development of robust devices, we investigate here the microscopic degradation pathways of $MAPbI_3$ microplates. Using *in situ* transmission electron microscopy to follow the thermal degradation process, we find that under moderate heating at 85°C the crystalline structure shows a gradual evolution from tetragonal $MAPbI_3$ to trigonal lead iodide layered crystals with a fixed crystallographic direction. Our solid-state nudged elastic band calculations confirm that the surface-initiated layer-by-layer degradation path exhibits the lowest energy barrier for crystal transition. We further show experimentally and theoretically that encapsulation of the perovskites with boron nitride flakes suppresses the surface degradation, greatly improving its thermal stability. These studies provide mechanistic insight into the thermal stability of perovskites that suggests new designs for improved stability.

INTRODUCTION

Organolead halide perovskite ($CH_3NH_3PbX_3$, X = Cl, Br, I) materials have shown great promise for high-efficiency, low-cost, and solution-processable solar cells.[1–15] However, their poor environmental and thermal stabilities represent a major barrier to practical applications of perovskite solar cells. For instance, the most popular methylammonium lead tri-iodide ($MAPbI_3$) perovskite solar cell material[5,12,16–19] suffers from instability upon exposure to humidity[20–24] or moderate temperature increases.[9,20,24,25] Although hermetically sealed packaging could deter the humidity-induced degradation, the thermal-induced degradation remains a key challenge for the viability of perovskite solar cells, especially under continued exposure to sunlight. Recent reports show that the thermal stability of the $MAPbI_3$ is considerably affected by the fabrication routes used to make perovskite solar cell devices.[20,24] However, the atomistic mechanism for the structure evolution of the perovskite hybrid structure during the heating process remains elusive. We report here an *in situ* transmission electron microscopy (TEM) study[26,27] of the thermal degradation of $MAPbI_3$ using an environmental gas cell that dynamically monitors the thermal-induced degradation under controlled gas flow. By continuously monitoring the crystalline structure in reciprocal space, we find a gradual evolution from tetragonal $MAPbI_3$ to trigonal lead iodide (PbI_2) layered crystals with a fixed crystallographic direction under moderate heating at 85°C. To understand the

Context & Scale

The organolead halide perovskites have shown extraordinary potential for low-cost solution-processable photovoltaic devices, with the power conversion efficiency rapidly soaring beyond 20%. However, the perovskite devices today are generally plagued by their poor environmental and thermal instability, and the atomistic mechanism for the thermal degradation remains largely unexplored. Here we report a systematic *in situ* transmission electron microscopy investigation of perovskite structure transition at 85°C. Along with theoretical calculations, we discover a surface reaction initiated layer-by-layer degradation pathway during the $MAPbI_3$ perovskite thermal degradation. Based on this finding, we developed a strategy using few-layer hBN encapsulation to restrain the surface reaction and thus considerably improve the thermal stability. This work reveals the atomistic pathway of perovskite structure evolution under heating and suggests a potential strategy for creating perovskite devices with improved stability.

CrossMark

kinetics of this process, we determined the energy barriers of the $MAPbI_3$ thermal degradation, using the solid-state nudged elastic band (ssNEB) method[28,29] with the Perdew-Burke-Ernzerhof (PBE) flavor[30] of density functional theory (DFT). The DFT calculations confirm that surface degradation leads to a low energy barrier pathway for crystal structure transitions, suggesting a layer-by-layer degradation pathway starting from the crystal surface. This demonstration of the crystalline structure evolution of perovskite $MAPbI_3$ during thermal-heating-induced degradation provides important mechanistic insights for resolving the critical stability hurdle in practical applications of perovskite solar cells. We further show experimentally that encapsulation of the perovskites with boron nitride (BN) flakes greatly suppresses surface degradation of the perovskite, significantly improving its thermal stability.

RESULTS

The $MAPbI_3$ used in our study was synthesized by intercalating highly crystallized two-dimensional (2D) layered PbI_2 microplates with methylammonium iodide (MAI).[31,32] During the experiment, perovskite stability was tested in the TEM gas holder (Figure S1) with continuous *in situ* heating at 85°C, the temperature standard in International Electrotechnical Commission 61646 photovoltaic solar testing specification for evaluating the long-term stability of solar cells.[33] We continuously monitored the real-space TEM image of $MAPbI_3$ microplates (inset i in Figure S1B) and the corresponding electron diffraction (ED) patterns (inset ii in Figure S1B) during the heating process. The TEM beam current density was maintained at a low dose of 1.12×10^3 A/m^2 for high-resolution TEM (HRTEM) imaging (Titan TEM, FEI, operating at 200 kV) and 32 A/m^2 during the ED pattern acquisition, to prevent irradiation damage of the specimen and ensure that we observed the intrinsic behavior of the crystalline structure transition under thermal loading. A control experiment conducted under identical condition without thermal loading shows that no obvious structural change is observed, suggesting that the beam damage has little influence during *in situ* observations (Figure S3).

Figure 1A shows a detailed crystalline phase of the pristine $MAPbI_3$. Before thermal degradation, the perovskite specimen is sealed in a gas cell at room temperature (20°C). At this point it exhibits tetragonal crystal structure (a = b = 8.8 Å, c = 12.7 Å).[34] By matching the measured lattice spacing in selected-area electron diffraction (SAED) patterns (Figure 1B) with diffraction peaks observed in X-ray diffraction (XRD) pattern (Figure S4), we can index the set of lattice planes (2-20) and (220), and identify the [001] axis (the c axis) as the normal direction of perovskite $MAPbI_3$ microplate (details of the indexing process are described in Experimental Procedures). Then, as the specimen is heated at 85°C for about 400 s in vacuum, the lattice spacing and the angle of tetragonal lattice fringes undergo a fundamental transformation (Figure 1C). The resulting SAED pattern in the reciprocal space reveals a six-fold symmetric pattern (Figure 1D) with a *d* spacing of 4.4 Å, consistent with trigonal crystalline structure of layered PbI_2.[32,35] PbI_2 is the commonly seen by-product of the moisture-induced $MAPbI_3$ degradation.[21,23,36,37] The six-fold trigonal structure of the final products indicates that the normal direction of this structure is also [001].

We further carried out the *in situ* heating of $MAPbI_3$ in static dry air ambient with chamber pressure of 700 torr. We used the Airgas UN 1002 Ultra-Zero-Certified compressed air for the experiment, the water content here being lower than 2 ppm. Continuously tracking the structure evolution of an individual $MAPbI_3$ grain

[1]Department of Materials Science and Engineering, University of California, Los Angeles, CA 90095, USA

[2]Department of Chemistry and Biochemistry, University of California, Los Angeles, CA 90095, USA

[3]Materials and Process Simulation Center (MC139-74), California Institute of Technology, Pasadena, CA 91125, USA

[4]California NanoSystems Institute, University of California, Los Angeles, CA 90095, USA

[5]These authors contributed equally

[6]Lead Contact

*Correspondence: wag@wag.caltech.edu (W.A.G.), yhuang@seas.ucla.edu (Y.H.), xduan@chem.ucla.edu (X.D.)

http://dx.doi.org/10.1016/j.joule.2017.08.005

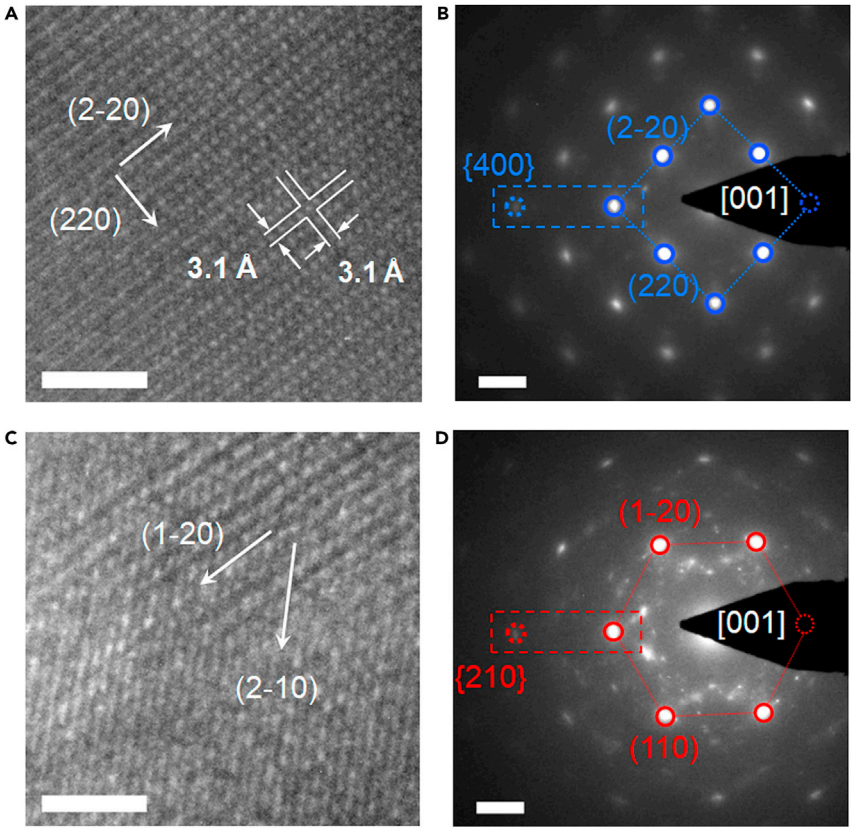

Figure 1. Crystalline Structures of $MAPbI_3$ before and after the Thermal Effect

(A) HRTEM image of the pristine $MAPbI_3$ with clearly resolved lattice fringes. The lattice spacing is measured as 3.11 Å. Scale bar, 2 nm.

(B) The SAED pattern of pristine $MAPbI_3$in reciprocal space. Scale bar, 2 nm^{-1}.

(C and D) HRTEM image of the $MAPbI_3$ after heating (C; scale bar, 2 nm), and the corresponding ED pattern (D; scale bar, 2 nm^{-1}).

allows us to probe the microscopic degradation pathway. As shown in Figures 2A–2C, upon baking at 85°C for about 60 s, we identify a new hexagonal/trigonal crystalline phase that gradually expands from the pristine square lattice phase (Figure 2B). At 100 s, about 75% of the original phase is converted to the hexagonal/trigonal phase material, which is most likely trigonal PbI_2 (Figure 1D). By tracking the evolution of the crystalline structures, we find the same evolution pathway for $MAPbI_3$ under dry air or vacuum ambient, particularly the clearly correlated evolution of the {400} set of planes in the tetragonal pattern (Figures 1B and 1D) and the {210} planes in the trigonal pattern (inset in Figures 2A and 2C) (discussed in detail below). Therefore, we conclude that both in dry air and ambient vacuum, the thermal effect is the sole dominant cause for degradation of the $MAPbI_3$ perovskite.[20,24,38] Importantly, the diffraction pattern shows transformation from one single crystalline pattern to another, indicating a direct transition between the two structures without significant disordering.

The crystalline structure decomposition pathway under thermal heating is likely different from moisture-induced degradation because (1) the decomposition is not initiated by the intrinsic hygroscopicity of alkylammonium cations[22,24] but solely from thermally induced processes, and (2) no $MAPbI_3$ hydrates are generated during the degradation process.[22,39,40] Although one cannot absolutely exclude the slight

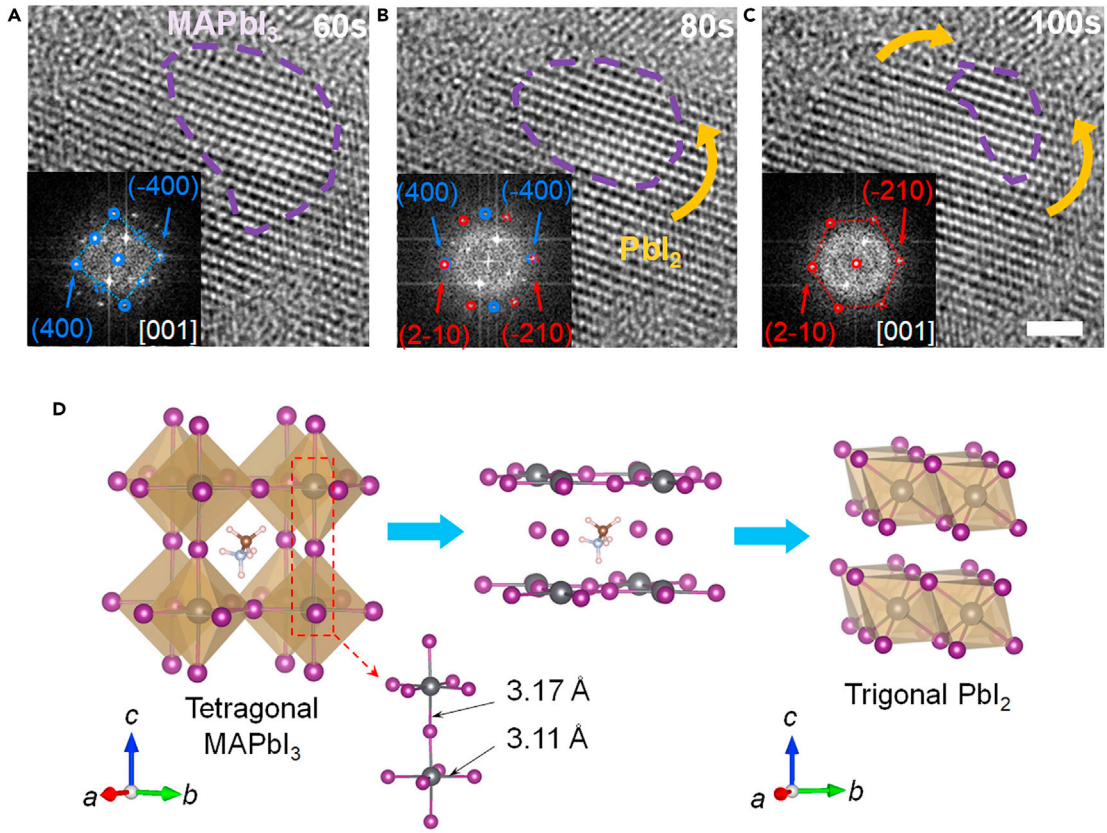

Figure 2. Direct Transition from Tetragonal to Trigonal Crystalline Structure

(A–C) Degradation process of an individual $MAPbI_3$ grain. The purple dashed lines in (A), (B), and (C) outline the shrinking perovskite grain as it degrades to PbI_2. Insets: FFT phase diagrams of the corresponding HRTEM images. Scale bar, 2 nm.

(D) Transition from $MAPbI_3$ with a tetragonal configuration to PbI_2 with a trigonal configuration. In pristine $MAPbI_3$, the Pb-I bond along the c axis has a length of 3.17 Å, slightly longer than those along the a and b axis (3.11 Å). As the longer Pb-I bonds break due to external stimulus, the PbI_2 2D planar structure transforms to the trigonal configuration, followed by the escape of methylammonium iodide.

effect of water on degradation in ambient dry air, we believe the role of the water has been largely limited in our experiment since degradation behavior in dry air shows a direct transition between two single crystalline structures (tetragonal and trigonal) without the generation of amorphous $MAPbI_3$ hydrate.

Our analysis of the corresponding fast Fourier transform (FFT) crystalline phase transition during the thermal degradation provides two important implications. First, the tetragonal $MAPbI_3$ perovskite thermal degradation is the reverse of its synthesis process. As introduced in the previous paragraph, the highly crystallized layered PbI_2 is the starting material for synthesizing $MAPbI_3$.[16,31,32,41] The intercalation of MAI causes twisting of the corner sharing PbI_6 octahedron in the 2D layered PbI_2 structure and forming of Pb-I-Pb bonds between the PbI_2 layers (Figure 2D).[32] The as-synthesized $MAPbI_3$ exhibits a three-dimensional framework with PbI_6 octahedron inorganic cages that encapsulates organic methylammonium cations.[31] Previous research reported that in the tetragonal configuration of $MAPbI_3$, the Pb-I-Pb bonds along the [001] direction of $MAPbI_3$ are slightly longer, by 0.06 Å, than those in the (001) plane (Figure 2D),[34,42] which indicates weaker bond strengths and thus less resistance to bond breakage.[43] Thus, it is expected that this bond tends to break first under external stimulus. Figure 2D schematically shows the simulated

$MAPbI_3$ thermal degradation process. As the Pb-I-Pb bonds break along the [001] direction, $CH_3NH_3^+$ and I^- are released and the remaining PbI_2 planes transit simultaneously to the PbI_2 trigonal structure. We expect the released $CH_3NH_3^+$ and I^- to escape in the form of CH_3NH_2 and HI gas molecules owing to their favorable free energies. Therefore, the thermal-induced $MAPbI_3$ degradation can be expressed as:

$$MAPbI_{3\ solid} \rightarrow PbI_{2\ solid} + [CH_3NH_3^+ + I^-] \rightarrow PbI_{2\ solid} + CH_3NH_{2\ gas} + HI_{gas}$$

(Equation 1)

Second, we note that both the SAED patterns (Figures 1B and 1D) and the FFT patterns (insets in Figures 2A–2C) show persistent diffraction spots during the degradation process. As shown in Figures 1B and 1D, although the crystal lattice symmetry changes from tetragonal to trigonal, the diffraction spots (2-10) in the trigonal structure (Figure 1D) remain at the exactly same location as the diffraction spots (400) in the tetragonal phase (Figure 1B). Identical diffraction spots in trigonal SAED pattern are observed along the [2-10] direction, including the series of planes in this direction. Therefore, we conclude that the set of {400} crystalline planes along the [400] direction in tetragonal $MAPbI_3$ are identical to the {210} facets along the [2-10] direction in the transited trigonal PbI_2 structure. The identity of crystalline facets indicates an equivalence of lattice spacing along <400>/<210> direction during the crystal structure transition, providing important insight into the conversion pathway.

To further probe the crystal structure transformation pathway, we characterized *in situ* the evolution from tetragonal $MAPbI_3$ to trigonal PbI_2 in reciprocal space. Figure 3A shows sequential SAED pattern snapshots during $MAPbI_3$ degradation in vacuum. At the beginning (20 s), the observed tetragonal $MAPbI_3$ pattern along the [001] axis allows indexing of the diffraction spots as: (400), (−400), (220), (−220), and (040) (see the indexing process in Experimental Procedures). The evolution of crystalline structure starts as thermal energy is applied, and the pristine tetragonal pattern gradually evolves into the PbI_2 trigonal pattern (~20 s to 220 s). With continued heating, the tetragonal pattern eventually transforms to the standard PbI_2 trigonal pattern (at 420 s). The direct transformation of {400} facets in the tetragonal phase to {210} facets in the trigonal phase with retained diffraction intensity and spatial location is obvious before and after the degradation. However, the location and intensity of other diffraction spots change, which indicates the drifting of corresponding facets and the distortion of crystalline structure.

We quantified the $MAPbI_3$structure evolution in the reciprocal space by plotting the intensity dynamics of the key diffraction spots as a function of time. Figure 3B shows that, in the tetragonal structure, the diffraction intensity peaks for the (220), (2-20), and (004) planes decrease continuously with increasing heating time, while the (110) and (−120) planes in the trigonal structure are growing at a similar rate (Figure 3C). Based on the peak intensity plots, the evolution of the SAED pattern from tetragonal to trigonal phase shows a clear sequential transition process. Especially at 220 s, we see clearly the overlapped diffraction pattern along the <400> of the perovskite and the <2-10> of the trigonal (Figure 3A). As discussed previously (Figure 2D), the breaking of the Pb-I-Pb bond along the [001] direction initiates $MAPbI_3$ degradation, after which the suspended PbI_2 planes transit into the trigonal structure. The largely overlapping single crystal SAED patterns, as well as the intensity peak dynamics (Figures 3B and 3C), suggest strongly a stacked crystalline architecture of tetragonal and trigonal phase during the degradation process, and

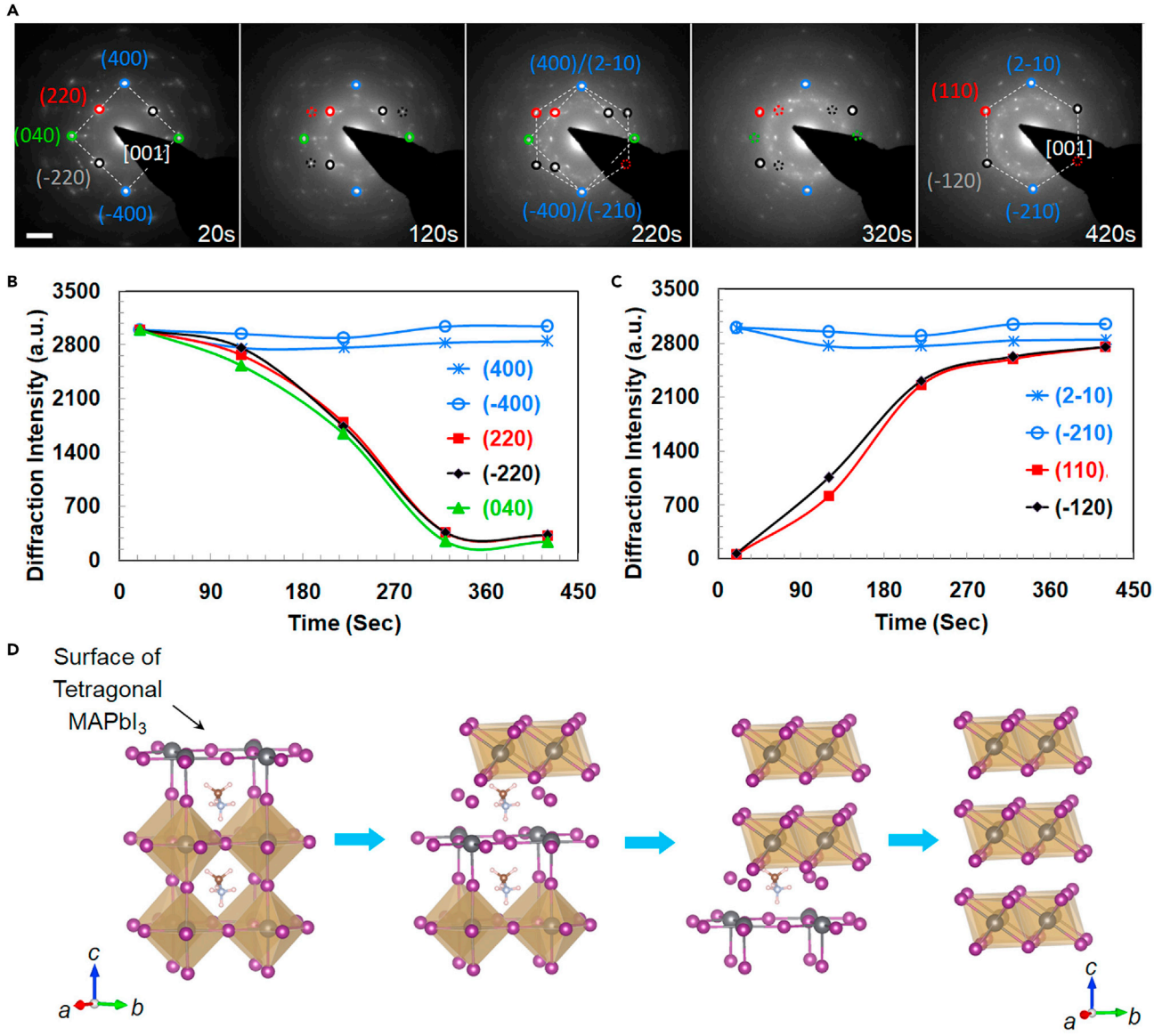

Figure 3. The Structural Evolution from Tetragonal Configuration to Trigonal Configuration

(A) *In situ* monitoring of the structure evolution of $MAPbI_3$ in reciprocal space. After 400 s heating at 85°C, the SAED patterns of $MAPbI_3$ transform completely from tetragonal to trigonal symmetry. Scale bar, 2 nm^{-1}.

(B and C) Measured diffraction spot intensities as a function of time for the tetragonal (B) and trigonal (C) phase.

(D) Schematic illustration of the layer-by-layer degradation of $MAPbI_3$ to produce the stacked trigonal/tetragonal structure with preserved crystallographic orientation. The surface of tetragonal $MAPbI_3$ is transitioning one by one to PbI_2 layers, exposing the underlying layer as the new surface layer as degradation progresses.

the thickness ratio between these two phases varies with heating time. For example, during the beginning of degradation (0–120 s) the tetragonal structure takes the dominant proportion in the stacked structure, so the SAED pattern shows a tetragonal phase. With continued heating the thickness of the PbI_2 layers increases, and eventually becomes the major proportion in the stacked structure (~420 s).

To gain further insight on the atomistic details of the $MAPbI_3$ thermal degradation pathway, it is critical to determine the reaction modes by considering the relevant

energy barriers. Either bulk reactions or surface reactions could be responsible for the observed thermal transformation from tetragonal to trigonal phase. In the bulk reaction, the crystalline structure reacts homogeneously,[44,45] with all weak Pb-I bonds along [001] breaking simultaneously during the decomposition. However, the surface reaction can take place in a sequential layer-by-layer style starting from the surface.[46] Intuitively, this reaction mode is more favorable for thermal degradation than the bulk reaction for two reasons: (1) the surface state is generally less stable than the bulk counterpart because of dangling bonds and reconstruction (structure relaxation and charge redistribution) present on the surface, making it energetically more favorable for thermal motions to trigger the decomposition, and (2) the lattice transition from the tetragonal to trigonal phase associated with surface degradation leads to less strain on the free surface, whereas within the bulk the periodicity enforces large strain from either direction.

We carried out DFT calculations with the functional PBE using the ssNEB technique[28,29,47] to locate the minimum energy path from tetragonal $MAPbI_3$ to the PbI_2 layered structure (see Experimental Procedures). The empirical D3 dispersion correction[48,49] was also applied to account for the van der Waals attraction (London dispersion) interactions important in the $MAPbI_3$ structure but missing in PBE.[50] We found that the volume decomposition along the [001] direction enables the lowest energy path (versus other directions in bulk reaction). As shown in Figure S5, the decomposition barrier of [001] for bulk decomposition is 0.43 eV per $MAPbI_3$ unit, which is about 0.07 eV lower than that along [−110], corresponds to a 15-fold faster reaction rate (estimated using transition state theory, rate = $(kT/h)\exp(-\Delta G^{\dagger}/kT)$).

We also used DFT to investigate the role of the surface in the decomposition process, with a two-layer slab model of (001) tetragonal $MAPbI_3$ surface as a starting structure and a trigonal PbI_2 plus released MAI as a final product. Figure 4A shows the surface degradation energy path between initial tetragonal phase and final trigonal phase. We find that the barrier for decomposition started with the surface is only 0.26 eV per $MAPbI_3$ unit, corresponding to a reaction rate ~1,000-fold faster than that of the intrinsic bulk decomposition along the [001] pathway (estimated by transition state theory). This indicates that the surface reaction is kinetically preferred compared with bulk degradation. Degradation of the surface layer exposes the next surface layer underneath to drive the decomposition sequentially throughout the entire bulk in a layer-by-layer fashion, eventually leading to the degradation of $MAPbI_3$ bulk. Figure 4B shows the simulated transition process of an individual $MAPbI_3$ layer by selected reaction coordinates. The simulation indicates that (1) the surface transition shows a contraction mode, and (2) the contraction occurs along [100] direction.

Our predicted surface reaction path of the $MAPbI_3$ from the DFT calculations allows generation of a stacked tetragonal-trigonal crystalline structure. During the structure transition, the {400} planes in tetragonal and the {210} planes in trigonal are precisely matched (Figure 3A). The transition of $MAPbI_3$ to PbI_2 in real space indicates contraction of each suspended PbI_2 along the a axis to form the trigonal structure (Figure 4C). Since each layer of $MAPbI_3$ follows a layer-by-layer contraction reaction and the surface transition guarantees the sequential reaction along the c axis ([001] direction), an overlapped tetragonal $MAPbI_3$and trigonal PbI_2 crystalline structure in reciprocal space is expected during the reaction, as shown in Figure 3D. Indeed, the surface reaction on $MAPbI_3$ is consistent with the crystalline structure evolution in the reciprocal space, as we have observed *in situ* (Figure 3A).

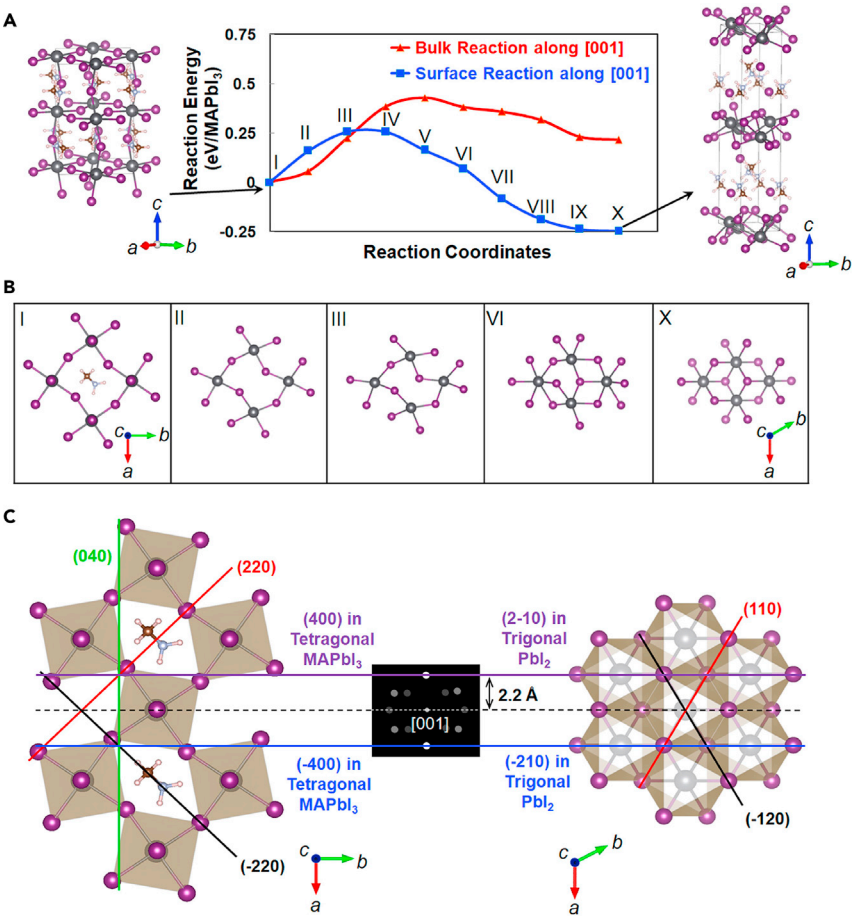

Figure 4. The DFT Calculated Minimum Energy Path for $MAPbI_3$ Thermal Degradation

(A) The reaction energy profiles are calculated by the ssNEB method. The saddle point is 0.26 eV for surface degradation and 0.43 eV for bulk degradation along the [001] axis.

(B) Selected transition states of an individual PbI_2 layer during the surface reaction. The evolution of the structure shows contraction of the $MAPbI_3$ layer along the a axis ([100] direction) to form a PbI_2 layer.

(C) Precise match of pristine $MAPbI_3$ layer and the resulting PbI_2 layer along {400}/{120} planes. Based on the location of diffraction spots in reciprocal space, the overlap of diffraction patterns during the structure evolution could be viewed as a match of $MAPbI_3$ and PbI_2 layer in {400}/{120} facets along the a axis.

Using the surface reaction as the main pathway for the perovskite $MAPbI_3$ thermal degradation, we can estimate the reaction rate constant using transition state theory:

$$\lambda = \frac{k_B T}{h} e^{-\frac{\Delta G}{k_B T}}, \qquad \text{(Equation 2)}$$

where k_B is Boltzmann's constant, T is the heating temperature, h is Planck's constant, and $\Delta G = \Delta H - TS$ is the free energy barrier of surface degradation. Here the DFT calculations lead to ΔE that must be corrected for vibrational effects (zero point energy and specific heat) to obtain ΔH and ΔS. We approximated ΔG with the electronic energy ΔE from DFT calculations, thereby ignoring the contributions from the zero point energy of the phonon modes, the phonon contributions to the specific heat (needed to integrate ΔH from 0 K to 298 K), and the entropy. We note that the entropy of soft phonons in $MAPbI_3$ likely contributes to its phase

transitions,[51] which might alter the values estimated here, but should not change the qualitative conclusions, because the free energy landscape of degradation studied here is dominated by strong chemical bonding changes (electronic effects). Including these contributions would further lower the barriers, which arise from bond breaking and disorder present in the transition states. Consequently we consider that our predicted reaction rates provide lower bounds. The surface degradation rate can be estimated using

$$v = A \cdot \lambda, \qquad \text{(Equation 3)}$$

where A is the surface area of an individual $MAPbI_3$ octahedron. At $T = 85^{\circ}C$ the surface energy barrier $\Delta E = 0.26$ eV leads to a degradation rate of 77.7 $\mu m^2/s$. For an individual $MAPbI_3$ microplate with area of 100 μm^2 and 200 nm thickness, and considering the 6.5 Å height of $MAPbI_3$ octahedral, we estimate that it will take ~400 s to complete the entire transformation process, which is consistent with the time range (400–500 s) observed by our *in situ* studies (Figure 3A). This further confirms that the surface reaction plays a primary role during the thermal degradation.

DISCUSSION

Our *in situ* TEM observations and the DFT simulations show that the thermal-induced degradation starts at the surface of $MAPbI_3$ and progresses in a layer-by-layer fashion. This new insight suggests that it would be possible to suppress the layer-by-layer thermal degradation of $MAPbI_3$ bulk by restraining the structure transition of the surface layer. To this end, we employed hexagonal boron nitride (hBN) thin flakes as the encapsulation layer on $MAPbI_3$ surface and fabricated a BN-perovskite-BN heterostructure (Figures 5A–5C and S6).[52–55] We conducted *in situ* characterization of the hBN-perovskite-hBN heterostructure in vacuum at 85°C using the same protocols described above. We demonstrated that encapsulated hBN shows considerably improved thermal stability. In particular, no obvious structural change is observed after 30 min of continuous heating at 85°C (Figure 5D), in stark contrast to the rapid emergence of the trigonal phase within 1 min and the complete transformation to trigonal PbI_2 within 7 min of the same thermal treatment for the non-encapsulated tetragonal perovskites (Figure 3A).[56]

We next conducted DFT simulations to understand the fundamental factors responsible for the improved stability by BN encapsulation. The as-calculated minimum energy path indicates that the energy reaction barrier of the $MAPbI_3$surface with hBN capping is about 0.05 eV higher than the pristine $MAPbI_3$ under thermal loading (Figure S7), corresponding to a 7-fold slower reaction rate. The calculated deceleration rate is consistent with the experiment results as illustrated in Figure 5D. Such stabilization from hBN encapsulation is rationalized as follows. The initial $MAPbI_3$ surface has Pb^+ and I^- dangling bonds, atoms that are no longer stabilized by the PbI_2 layer as in the bulk. Thus they are more susceptible to rearrange under even moderate thermal excitation, triggering the decomposition from the surface. With BN encapsulation of the perovskite, the B^+ and N^- in the hBN interact with perovskite surface dangling bonds with considerable orbital overlap and charge transfer, as demonstrated by our DFT calculations (Figure S8A). Such interaction between charges in hBN (B^+ and N^-) and dangling bonds (Pb^+ and I^-) reduces the surface activity, retarding surface degradation and improving the overall stability of the material. These experimental and computational studies confirm that surface reactions play a critical role in thermal degradation on the $MAPbI_3$ that is effectively countered by encapsulation with a thin hBN layer on the free surface. We suggest that this approach of employing 2D nanoflakes providing charge alternations,

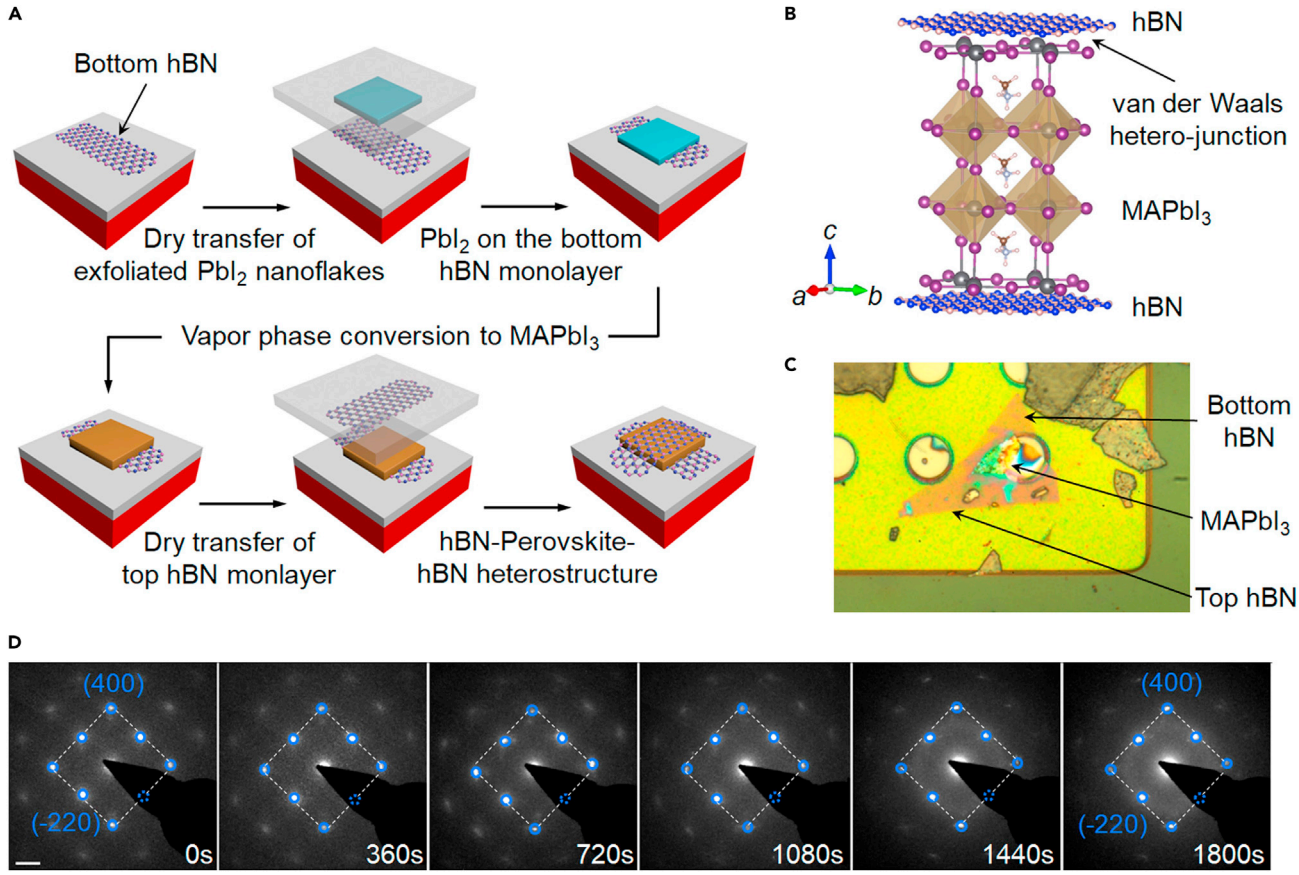

Figure 5. The Thermal Stability Characterization of $MAPbI_3$ with Surface Protection by a BN Thin Layer

(A) BN-perovskite-BN heterostructure fabrication process.

(B) Schematic of the BN-perovskite-BN heterostructure.

(C) The BN-perovskite-BN heterostructure on a gas cell bottom chip.

(D) $MAPbI_3$ with surface protection shows robust thermal stability. The thermal energy (85°C in vacuum) has not affected the crystalline structure of the $MAPbI_3$ in 30 min of heating. Scale bar, 2 nm^{-1}.

such as hBN or transition metal dichalcogenides (TMDs), to prevent surface reactions could be applied to many other environmental sensitive hybrid perovskites with surface dangling bonds. In addition to improving the stability of the perovskite structure, these 2D thin layers (e.g., graphene, hBN, TMDs) have promising potential for tuning the electronic states of the perovskites.[57,58] Thus, we expect that development of perovskite/2D heterostructures might offer significant potential for tailoring the photoelectrical performance and environmental stabilities of perovskite-based devices. Together, our investigations validate the thermal degradation model to explain these observations and suggest new strategies for promoting the stability of perovskites that are critical for practical applications of perovskite photoelectrochemical materials and devices.

EXPERIMENTAL PROCEDURES

Synthesis of $MAPbI_3$ Perovskites

$MAPbI_3$ was synthesized by intercalating MAI into solution-grown PbI_2 microplates.[32] Diluted PbI_2 solution at 80°C with a concentration of 0.1 g/100 mL was dropped on the bottom E-chip of a TEM gas cell to seed the chip for subsequent growth. The seeded chip was immersed in a saturated PbI_2 solution (~0.3 g/100 mL)

with a starting temperature of 80°C for continued growth into large microplates as the temperature was dropped slowly. The chip was taken out from the solution when growth was complete.

The as-grown PbI_2 microplates were converted to $MAPbI_3$ by using intercalation reaction in a home-built chemical vapor deposition (CVD) system.[31,32] MAI was synthesized following a reported solution method.[59] MAI precursor was placed in the center zone of a tube furnace where the temperature is set to 120°C, and the chip with PbI_2 microplates grown on it was placed in the downstream (5–6 cm from the MAI precursor) where temperature was about 110°C. The pressure of the tube was maintained at 125 mbar. Argon flow was employed to carry the vaporized MAI to PbI_2 microplates. PbI_2 microplates were completely converted to $MAPbI_3$ within 12 hr of intercalation treatment.

The *In Situ* Environmental System

We use an ATMOSPHERE 200 *in situ* heating and gas reaction system from Protochips to carry out *in situ* characterization. As shown in Figure S1, the combination of top and bottom E-chip forms a gas cell. E-chips integrate a thin, durable amorphous silicon nitride window and a silicon carbide-based ceramic thin-film heating membrane to provide a strong barrier for containing gases with minimal electron beam scatter. The gas cell for the *in situ* studies was sealed very quickly (~2 min) after removing from the CVD system, and connected to the Atmosphere system for further pump and purge to ensure a clean environment. The inner pressure of the gas cell was maintained at 1 torr after the pumping process.

The temperature applied to the chip was applied by joule heating. A ceramic heating membrane was employed to heat the sample. For the temperature stabilization during the experiment, a resistance-versus-temperature calibration file was generated for every E-chip to calibrate the heating temperature. This file was loaded into the Atmosphere Clarity software. The stabilization time was acquired by monitoring the resistance of the E-chip as it was heated. It settled very quickly, in less than 1 s. The temperature was constantly monitored by the software using a feedback loop. The temperature accuracy of the gas cell was 5% and was tested with known samples, such as materials with a well-known melting point. The sample viewing area (holes in the silicon carbide membrane) has a very uniform temperature (Figure S2), as shown by optical pyrometer temperature map provided by Protochips.

For *in situ* studies, the electron beam current density was restricted to 32 A/m^2 and the electron beam irradiation rate remained as low as ~100 e/nm^2 s, to minimize the beam effect on the specimen. A control experiment was conducted under exactly the same conditions without thermal loading to probe the electron beam damage during *in situ* observations. No apparent crystalline structure evolution of $MAPbI_3$ was observed after 600 s of electron beam irradiation (Figure S3), suggesting that the beam has little influence on the observed sample, which guarantees the intrinsic performance of the $MAPbI_3$ perovskite under thermal effect.

X-Ray Diffraction Characterization and Index of the Electron Diffraction Pattern

XRD characterization of microplates before the conversion showed characteristic diffraction peaks of 2-H PbI_2 crystals (Figure S4), indicating the highly crystallized

structure of the plate.[60] After the conversion, all of the PbI_2 peaks disappeared and all of the peaks matching the $MAPbI_3$ perovskite pattern appeared,[61,62] confirming the complete conversion of the microplates.

For the 2-H $PbI_2$with a trigonal crystalline structure, the ED pattern could be indexed by adding the vectors. As we indexed the diffraction spots ($h_1k_1l_1$) and ($h_2k_2l_2$) in Zero Order Laue Zone (ZOLZ) as (100) and (010), respectively, the rest of the spots could be determined. As shown in Figure 3C, ($h_3k_3l_3$) could be indexed by adding ($h_1k_1l_1$) and ($h_2k_2l_2$), which produced (110). By using the same approach, ($h_4k_4l_4$) could be determined as (1-20). The view axis was [001].

For the $MAPbI_3$ with a tetragonal crystal system, the lattice spacings of $MAPbI_3$ were measured (from XRD) as $d_1 = d_2 = 3.11$ Å, $d_3 = 2.2$ Å. Based on these lattice spacings, the observed ED pattern was indexed as ($h_1'k_1'l_1'$) → (2-20), ($h_2'k_2'l_2'$) → (220), and ($h_3'k_3'l_3'$) → (400). The viewing axis was confirmed as [001].

The Preparation of hBN-Perovskite-hBN Heterostructure in an E-Chip

As shown in Figure S6, few-layer hBN was first transferred onto the E-chip and used as bottom substrate of the perovskite. In parallel, a layer of polymethylmethacrylate (PMMA) was spun coated on a silicon substrate, followed by coating another layer of polypropylene carbonate (PPC). The PbI_2 with a thickness of 50–80 nm was exfoliated onto the PMMA/PPC polymer stack. The polymer stack was then peeled off from the silicon substrate and attached to a PDMS (polydimethylsiloxane) stamp with PbI_2 side facing up. The PDMS stamp with PbI_2 sitting on the PMMA/PPC stack was positioned on the bottom hBN on the E-chip. PDMS and PbI_2 were then brought into contact with BN. The polymer stack was released from the PDMS stamp by heating the substrate to 120°C. After transfer, the polymer stack was dissolved in chloroform for 10 min. The PbI_2 sitting on the hBNs was then converted into perovskite using vapor-phase reaction with MAI vapor carried by argon gas flow. Another few-layer hBN serving as top cover was prepared on another PMMA-covered silicon substrate, which was transferred immediately on the as-converted perovskite by the same method described above to obtain the hBN-perovskite-hBN heterostructure on an E-chip.

First-Principle Simulations of the Thermal Degradation of the $MAPbI_3$ bulk

To gain fundamental understanding of thermal decomposition of $MAPbI_3$ perovskite, we investigated the process using DFT. The calculations were performed with the VASP package,[63–65] using the PBE flavor[30] of DFT and the projector augmented wave method[66] to account for core-valence interactions. The empirical D3 dispersion correction[48,49] was included to account for van der Waals attraction (London dispersion) interactions important in the $MAPbI_3$ structure but missing in PBE.[50]

We used a 2 × 2 × 2 supercell to model the tetragonal phase and accommodate the structural transitions toward final products from decomposition, i.e., the trigonal PbI_2 layered structure plus the released MAI. The kinetic energy cutoff for plane wave expansions was set to 400 eV, and reciprocal space was sampled by the Γ-centered Monkhorst-Pack scheme with a grid of 2 × 2 × 2. We employed the ssNEB technique[28,29] with climbing image option[67] to locate the lowest energy pathways and, thus, the transition states. The final product structure was constructed by intercalating PbI_2 layered structure with MAI ion pairs and then relaxing both lattice and atomic positions. We found an intermediate compound that proceeds to the final decomposition by releasing weakly bound MAI as gas molecules, which is expected to be an entropy-driven process of low energy consumption and thus not the rate-determining step.

The intrinsic bulk decomposition was first studied along two characteristic directions [001] and [−110], which are aligned with the long and short Pb-I bonds, respectively. As shown in Figure S3, the decomposition barrier of [001] pathway is 0.43 eV per $MAPbI_3$ unit, lower by 0.07 eV than that of [−110] pathway, which corresponds to a 15-fold faster reaction rate (estimated by the Arrhenius equation). The kinetic dominance of [001] decomposition over [−110] counterpart is plausible because the Pb-I bonds along the [001] direction are longer by 0.06 Å than those along the [−110] direction, indicating weaker bond strengths and, thus, less resistance to bond breakage.

We also carried out the simulation of $MAPbI_3$ surface degradation with hBN encapsulation. The same setup as the pristine surface degradation was employed, with the difference that two hBN flakes were introduced by capping on both surfaces (Figure S7). The decomposition barrier of the $MAPbI_3$ surface with hBN capping was about 0.31 eV, 0.05 eV higher than the pristine $MAPbI_3$ surface under thermal loading (corresponding to a 7-fold slower reaction rate).

As a result, our study shows that the hBN 2D-thin-flake coverage was able to improve the integrity of the perovskite crystalline structure. The Pb^+ and I^- dangling bonds on the perovskite surface make them energetically more active under moderate thermal excitation, triggering the decomposition from the surface. By capping the $MAPbI_3$ surface with BN, the B^+ and N^- in the hBN could interact with perovskite surface dangling bonds with significant orbital overlap and charge transfer, as demonstrated by our theoretical calculations (Figure S8). Such interaction between charges in hBN (B^+ and N^-) and dangling bonds (Pb^+ and I^-) reduced the surface instability, retarding the surface degradation and improving the overall stability of the material.

SUPPLEMENTAL INFORMATION

Supplemental Information includes eight figures and can be found with this article online at http://dx.doi.org/10.1016/j.joule.2017.08.005.

AUTHOR CONTRIBUTIONS

X.D., Y.H., and Z. Fan designed the research and experimental studies. W.A.G. and H.X. designed and conducted the theoretical studies. Z. Fan carried out the *in situ* HRTEM characterization. H.X. performed the theoretical calculations. Y.W., G.W., and Z.L. synthesized the material and conducted the XRD characterization. Z. Feng and Z.Z. analyzed the data. H.C.-C., S.-J.L., and Z. Fan prepared the hBN-perovskite-hBN heterostructure. X.D., Z. Fan, and H.X. wrote the manuscript. All the authors participated in discussions of the research.

ACKNOWLEDGMENTS

X.D. acknowledges the support by National Science Foundation DMR1508144. Y.H. acknowledges the financial support from National Science Foundation EFRI-1433541. W.A.G. and H.X. acknowledge support by the Joint Center for Artificial Photosynthesis, a DOE Energy Innovation Hub, supported through the Office of Science of the U.S. Department of Energy under Award no. DE-SC0004993.

Received: June 15, 2017
Revised: June 24, 2017
Accepted: August 4, 2017
Published: September 20, 2017

REFERENCES

1. NREL chart, http://www.nrel.gov/ncpv/images/efficiency_chart.jpg, Accessed 13. 03, 2016.
2. McMeekin, D.P., Sadoughi, G., Rehman, W., Eperon, G.E., Saliba, M., Horantner, M.T., Haghighirad, A., Sakai, N., Korte, L., Rech, B., et al. (2016). A mixed-cation lead mixed-halide perovskite absorber for tandem solar cells. Science *351*, 151–155.
3. Yang, W.S., Noh, J.H., Jeon, N.J., Kim, Y.C., Ryu, S., Seo, J., and Seok, S.I. (2015). High-performance photovoltaic perovskite layers fabricated through intramolecular exchange. Science *348*, 1234–1237.
4. Chen, W., Wu, Y.Z., Yue, Y.F., Liu, J., Zhang, W.J., Yang, X.D., Chen, H., Bi, E.B., Ashraful, I., Gratzel, M., and Han, L.Y. (2015). Efficient and stable large-area perovskite solar cells with inorganic charge extraction layers. Science *350*, 944–948.
5. Zhou, H.P., Chen, Q., Li, G., Luo, S., Song, T.B., Duan, H.S., Hong, Z.R., You, J.B., Liu, Y.S., and Yang, Y. (2014). Interface engineering of highly efficient perovskite solar cells. Science *345*, 542–546.
6. Dou, L.T., Yang, Y., You, J.B., Hong, Z.R., Chang, W.H., and Li, G. (2014). Solution-processed hybrid perovskite photodetectors with high detectivity. Nat. Commun. *5*, 5404.
7. Burschka, J., Pellet, N., Moon, S.J., Humphry-Baker, R., Gao, P., Nazeeruddin, M.K., and Gratzel, M. (2013). Sequential deposition as a route to high-performance perovskite-sensitized solar cells. Nature *499*, 316–319.
8. Lee, M.M., Teuscher, J., Miyasaka, T., Murakami, T.N., and Snaith, H.J. (2012). Efficient hybrid solar cells based on meso-superstructured organometal halide perovskites. Science *338*, 643–647.
9. Heo, J.H., Im, S.H., Noh, J.H., Mandal, T.N., Lim, C.S., Chang, J.A., Lee, Y.H., Kim, H.J., Sarkar, A., Nazeeruddin, M.K., et al. (2013). Efficient inorganic-organic hybrid heterojunction solar cells containing perovskite compound and polymeric hole conductors. Nat. Photon. *7*, 487–492.
10. Liu, M.Z., Johnston, M.B., and Snaith, H.J. (2013). Efficient planar heterojunction perovskite solar cells by vapour deposition. Nature *501*, 395–398.
11. Noh, J.H., Im, S.H., Heo, J.H., Mandal, T.N., and Seok, S.I. (2013). Chemical management for colorful, efficient, and stable inorganic-organic hybrid nanostructured solar cells. Nano Lett. *13*, 1764–1769.
12. Kim, H.S., Lee, C.R., Im, J.H., Lee, K.B., Moehl, T., Marchioro, A., Moon, S.J., Humphry-Baker, R., Yum, J.H., Moser, J.E., et al. (2012). Lead iodide perovskite sensitized all-solid-state submicron thin film mesoscopic solar cell with efficiency exceeding 9%. Sci. Rep. *2*, 591.
13. Dou, L.T., Wong, A.B., Yu, Y., Lai, M.L., Kornienko, N., Eaton, S.W., Fu, A., Bischak, C.G., Ma, J., Ding, T.N., et al. (2015). Atomically thin two-dimensional organic-inorganic hybrid perovskites. Science *349*, 1518–1521.
14. Bush, K.A., Palmstrom, A.F., Yu, Z.J., Boccard, M., Cheacharoen, R., Mailoa, J.P., McMeekin, D.P., Hoye, R.L.Z., Bailie, C.D., Leijtens, T., et al. (2017). 23.6%-efficient monolithic perovskite/silicon tandem solar cells with improved stability. Nat. Energy *2*, 17009.
15. Bi, D., Yi, C., Luo, J., Décoppet, J.-D., Zhang, F., Zakeeruddin, Shaik M., Li, X., Hagfeldt, A., and Grätzel, M. (2016). Polymer-templated nucleation and crystal growth of perovskite films for solar cells with efficiency greater than 21%. Nat. Energy *1*, 16142.
16. Jeon, N.J., Noh, J.H., Kim, Y.C., Yang, W.S., Ryu, S., and Il Seol, S. (2014). Solvent engineering for high-performance inorganic-organic hybrid perovskite solar cells. Nat. Mater. *13*, 897–903.
17. Kim, H.S., and Park, N.G. (2014). Parameters affecting *I-V* hysteresis of $CH_3NH_3PbI_3$ perovskite solar cells: effects of perovskite crystal size and mesoporous TiO_2 layer. J. Phys. Chem. Lett. *5*, 2927–2934.
18. Kojima, A., Teshima, K., Shirai, Y., and Miyasaka, T. (2009). Organometal halide perovskites as visible-light sensitizers for photovoltaic cells. J. Am. Chem. Soc. *131*, 6050–6051.
19. Park, N.-G., Grätzel, M., Miyasaka, T., Zhu, K., and Emery, K. (2016). Towards stable and commercially available perovskite solar cells. Nat. Energy *1*, 16152.
20. Divitini, G., Cacovich, S., Matteocci, F., Cinà, L., Di Carlo, A., and Ducati, C. (2016). In situ observation of heat-induced degradation of perovskite solar cells. Nat. Energy *1*, 15012.
21. Niu, G.D., Guo, X.D., and Wang, L.D. (2015). Review of recent progress in chemical stability of perovskite solar cells. J. Mater. Chem. A *3*, 8970–8980.
22. Yang, J.L., Siempelkamp, B.D., Liu, D.Y., and Kelly, T.L. (2015). Investigation of CH3NH3PbI3 degradation rates and mechanisms in controlled humidity environments using in situ techniques. Acs Nano *9*, 1955–1963.
23. Rong, Y.G., Liu, L.F., Mei, A.Y., Li, X., and Han, H.W. (2015). Beyond efficiency: the challenge of stability in mesoscopic perovskite solar cells. Adv. Energy Mater. *5*, 1501066.
24. Conings, B., Drijkoningen, J., Gauquelin, N., Babayigit, A., D'Haen, J., D'Olieslaeger, L., Ethirajan, A., Verbeeck, J., Manca, J., Mosconi, E., et al. (2015). Intrinsic thermal instability of methylammonium lead trihalide perovskite. Adv. Energy Mater. *5*, 1500477.
25. Frost, J.M., Butler, K.T., and Walsh, A. (2014). Molecular ferroelectric contributions to anomalous hysteresis in hybrid perovskite solar cells. Apl Mater. *2*, 081506.
26. Nielsen, M.H., Aloni, S., and De Yoreo, J.J. (2014). In situ tem imaging of caco3 nucleation reveals coexistence of direct and indirect pathways. Science *345*, 1158–1162.
27. Cho, K.R., Kim, Y.Y., Yang, P.C., Cai, W., Pan, H.H., Kulak, A.N., Lau, J.L., Kulshreshtha, P., Armes, S.P., Meldrum, F.C., and De Yoreo, J.J. (2016). Direct observation of mineral-organic composite formation reveals occlusion mechanism. Nat. Commun. *7*, 10187.
28. Caspersen, K.J., and Carter, E.A. (2005). Finding transition states for crystalline solid-solid phase transformations. Proc. Natl. Acad. Sci. USA *102*, 6738–6743.
29. Sheppard, D., Xiao, P.H., Chemelewski, W., Johnson, D.D., and Henkelman, G. (2012). A generalized solid-state nudged elastic band method. J. Chem. Phys. *136*, 074103.
30. Perdew, J.P., Burke, K., and Ernzerhof, M. (1996). Generalized gradient approximation made simple. Phys. Rev. Lett. *77*, 3865–3868.
31. Ha, S.T., Liu, X.F., Zhang, Q., Giovanni, D., Sum, T.C., and Xiong, Q.H. (2014). Synthesis of organic-inorganic lead halide perovskite nanoplatelets: towards high-performance perovskite solar cells and optoelectronic devices. Adv. Opt. Mater. *2*, 838–844.
32. Wang, G., Li, D., Cheng, H.-C., Li, Y., Chen, C.-Y., Yin, A., Zhao, Z., Lin, Z., Wu, H., and He, Q. (2015). Wafer-scale growth of large arrays of perovskite microplate crystals for functional electronics and optoelectronics. Sci. Adv. *1*, 1500613.
33. International Electrotechnical Commission IEC 61646: Thin-film terrestrial photovoltaic (PV) modules—design qualification and type approval, 2nd Edition, 2008.
34. Brivio, F., Frost, J.M., Skelton, J.M., Jackson, A.J., Weber, O.J., Weller, M.T., Goni, A.R., Leguy, A.M.A., Barnes, P.R.F., and Walsh, A. (2015). Lattice dynamics and vibrational spectra of the orthorhombic, tetragonal, and cubic phases of methylammonium lead iodide. Phys. Rev. B *92*, 144308.
35. Li, D.H., Wang, G.M., Cheng, H.C., Chen, C.Y., Wu, H., Liu, Y., Huang, Y., and Duan, X.F. (2016). Size-dependent phase transition in methylammonium lead iodide perovskite microplate crystals. Nat. Commun. *7*, 11330.
36. Deretzis, I., Alberti, A., Pellegrino, G., Smecca, E., Giannazzo, F., Sakai, N., Miyasaka, T., and La Magna, A. (2015). Atomistic origins of $CH_3NH_3PbI_3$ degradation to PbI_2 in vacuum. Appl. Phys. Lett. *106*, 131904.
37. Leguy, A.M.A., Hu, Y., Campoy-Quiles, M., Isabel Alonso, M., Weber, O.J., Azarhoosh, P., van Schilfgaarde, M., Weller, M.T., Bein, T., Nelson, J., et al. (2015). Reversible hydration of Ch(3)Nh(3)PbI(3) in films, single crystals, and solar cells. Chem. Mater. *27*, 3397–3407.
38. Misra, R.K., Aharon, S., Li, B.L., Mogilyansky, D., Visoly-Fisher, I., Etgar, L., and Katz, E.A. (2015). Temperature- and component-dependent degradation of perovskite photovoltaic materials under concentrated sunlight. J. Phys. Chem. Lett. *6*, 326–330.
39. Frost, J.M., Butler, K.T., Brivio, F., Hendon, C.H., van Schilfgaarde, M., and Walsh, A. (2014). Atomistic origins of high-performance in hybrid halide perovskite solar cells. Nano Lett. *14*, 2584–2590.
40. Christians, J.A., Herrera, P.A.M., and Kamat, P.V. (2015). Transformation of the excited state and photovoltaic efficiency of $CH_3NH_3PbI_3$

perovskite upon controlled exposure to humidified air. J. Am. Chem. Soc. *137*, 1530–1538.

41. Chen, Q., Zhou, H., Hong, Z., Luo, S., Duan, H.-S., Wang, H.-H., Liu, Y., Li, G., and Yang, Y. (2014). Planar heterojunction perovskite solar cells via vapor-assisted solution process. J. Am. Chem. Soc. *136*, 622–625.

42. Ong, K.P., Goh, T.W., Xu, Q., and Huan, A. (2015). Structural evolution in methylammonium lead iodide $CH_3NH_3PbI_3$. J. Phys. Chem. A *119*, 11033–11038.

43. Pauling, L. (1954). The dependence of bond energy on bond length. J. Phys. Chem. *58*, 662–666.

44. Uhrich, K.E., Cannizzaro, S.M., Langer, R.S., and Shakesheff, K.M. (1999). Polymeric systems for controlled drug release. Chem. Rev. *99*, 3181–3198.

45. Tamada, J.A., and Langer, R. (1993). Erosion kinetics of hydrolytically degradable polymers. Proc. Natl. Acad. Sci. USA *90*, 552–556.

46. George, S.M., Yoon, B., and Dameron, A.A. (2009). Surface chemistry for molecular layer deposition of organic and hybrid organic-inorganic polymers. Acc. Chem. Res. *42*, 498–508.

47. Hratchian, H.P., and Schlegel, H.B. (2005). Finding Minima, Transition States, and Following Reaction Pathways on Ab Initio Potential Energy Surfaces (Elsevier Science Bv).

48. Grimme, S., Ehrlich, S., and Goerigk, L. (2011). Effect of the damping function in dispersion corrected density functional theory. J. Comput. Chem. *32*, 1456–1465.

49. Grimme, S., Antony, J., Ehrlich, S., and Krieg, H. (2010). A consistent and accurate ab initio parametrization of density functional dispersion correction (DFT-D) for the 94 elements H-Pu. J. Chem. Phys. *132*, 154104.

50. Lee, J.H., Bristowe, N.C., Bristowe, P.D., and Cheetham, A.K. (2015). Role of hydrogen-bonding and its interplay with octahedral tilting in $CH_3NH_3PbI_3$. Chem. Commun. *51*, 6434–6437.

51. Butler, K.T., Svane, K., Kieslich, G., Cheetham, A.K., and Walsh, A. (2016). Microscopic origin of entropy-driven polymorphism in hybrid organic-inorganic perovskite materials. Phys. Rev. B *94*, 180103.

52. Hadadian, M., Correa-Baena, J.-P., Goharshadi, E.K., Ummadisingu, A., Seo, J.-Y., Luo, J., Gholipour, S., Zakeeruddin, S.M., Saliba, M., Abate, A., et al. (2016). Enhancing efficiency of perovskite solar cells via N-doped graphene: crystal modification and surface passivation. Adv. Mater. *28*, 8681–8686.

53. Lee, Y., Kwon, J., Hwang, E., Ra, C.H., Yoo, W.J., Ahn, J.H., Park, J.H., and Cho, J.H. (2015). High-performance perovskite-graphene hybrid photodetector. Adv. Mater. *27*, 41–46.

54. Cheng, H.C., Wang, G.M., Li, D.H., He, Q.Y., Yin, A.X., Liu, Y., Wu, H., Ding, M.N., Huang, Y., and Duan, X.F. (2016). Van der Waals heterojunction devices based on organohalide perovskites and two-dimensional materials. Nano Lett. *16*, 367–373.

55. Li, D.H., Cheng, H.C., Wang, Y., Zhao, Z., Wang, G., Wu, H., He, Q., Huang, Y., and Duan, X. (2016). The effect of thermal annealing on charge transport in organolead halide perovskite microplate field-effect transistors. Adv. Mater. *29*, http://dx.doi.org/10.1002/adma.201601959.

56. Wang, Q., Chen, B., Liu, Y., Deng, Y., Bai, Y., Dong, Q., and Huang, J. (2017). Scaling behavior of moisture-induced grain degradation in polycrystalline hybrid perovskite thin films. Energy Environ. Sci. *10*, 516–522.

57. Niu, L., Liu, X.F., Cong, C.X., Wu, C.Y., Wu, D., Chang, T.R., Wang, H., Zeng, Q.S., Zhou, J.D., Wang, X.L., et al. (2015). Controlled synthesis of organic/inorganic van der Waals solid for tunable light-matter interactions. Adv. Mater. *27*, 7800–7808.

58. Ergen, O., Gilbert, S.M., Pham, T., Turner, S.J., Tan, M.T.Z., Worsley, M.A., and Zettl, A. (2017). Graded bandgap perovskite solar cells. Nat. Mater. *16*, 522–525.

59. Hao, F., Stoumpos, C.C., Cao, D.H., Chang, R.P.H., and Kanatzidis, M.G. (2014). Lead-free solid-state organic-inorganic halide perovskite solar cells. Nat. Photon. *8*, 489–494.

60. Zheng, Z., Liu, A.R., Wang, S.M., Wang, Y., Li, Z.S., Lau, W.M., and Zhang, L.Z. (2005). In situ growth of epitaxial lead iodide films composed of hexagonal single crystals. J. Mater. Chem. *15*, 4555–4559.

61. Baikie, T., Fang, Y., Kadro, J.M., Schreyer, M., Wei, F., Mhaisalkar, S.G., Graetzel, M., and White, T.J. (2013). Synthesis and crystal chemistry of the hybrid perovskite $(CH_3NH_3)PbI_3$ for solid-state sensitised solar cell applications. J. Mater. Chem. A *1*, 5628–5641.

62. Dong, Q., Fang, Y., Shao, Y., Mulligan, P., Qiu, J., Cao, L., and Huang, J. (2015). Electron-hole diffusion lengths >175 μm in solution-grown $CH_3NH_3Pbi_3$ single crystals. Science *347*, 967–970.

63. Kresse, G., and Hafner, J. (1993). Ab initio molecular dynamics for liquid metals. Phys. Rev. B *47*, 558.

64. Kresse, G., and Furthmuller, J. (1996). Efficiency of ab-initio total energy calculations for metals and semiconductors using a plane-wave basis set. Comput. Mater. Sci. *6*, 15–50.

65. Kresse, G., and Furthmuller, J. (1996). Efficient iterative schemes for ab initio total-energy calculations using a plane-wave basis set. Phys. Rev. B *54*, 11169–11186.

66. Kresse, G., and Joubert, D. (1999). From ultrasoft pseudopotentials to the projector augmented-wave method. Phys. Rev. B *59*, 1758–1775.

67. Henkelman, G., Uberuaga, B.P., and Jonsson, H. (2000). A climbing image nudged elastic band method for finding saddle points and minimum energy paths. J. Chem. Phys. *113*, 9901–9904.